

# Angle-Resolved Transport Measurements Reveal Electronic

## Nematicity in Cuprate Superconductors

J. Wu<sup>1</sup>, A. T. Bollinger<sup>1</sup>, X. He<sup>1,2</sup>, G. D. Gu<sup>1</sup>, M. Hu<sup>1</sup>, M. P. M. Dean<sup>1</sup>, I. K. Robinson<sup>1</sup>  
and I. Božović<sup>1,2</sup>

<sup>1</sup>*Brookhaven National Laboratory, Upton, New York 11973-5000, USA*

<sup>2</sup>*Yale University, Applied Physics Department, New Haven CT 06520, USA*

### **Abstract**

Observations of spontaneous breaking of the rotational symmetry in an electron fluid, the so-called ‘electronic nematicity’, has been reported in several quantum materials. We have developed several different methods, based on angle-resolved transport measurements, to determine the amplitude and the director of the nematic order. We present methods that are applicable to thin films or single crystals, illustrate them with transport data obtained on copper-oxide superconductors, and discuss their relative advantages and disadvantages.

**Keywords:** Electronic Nematicity, Copper Oxide Superconductor, Electrical transport

## 1. Introduction

Theorists have envisioned the existence of an intriguing new quantum state that spontaneously breaks the rotational symmetry of the electron fluid<sup>1-7</sup>. In analogy with liquid crystals, it was dubbed ‘electronic nematic’. It generally implies the presence of strong electron-electron correlations from which it ultimately originates. Evidence of broken rotational symmetry was indeed reported in two-dimensional electron gas (2DEG) systems in high magnetic fields<sup>8,9</sup>, strontium ruthenates<sup>10</sup>, copper oxide superconductors<sup>11-24</sup>, and Fe-based superconductors<sup>25-27</sup>. For example, our recent measurements of transport in thin films of the prototype copper-oxide superconductor,  $\text{La}_{2-x}\text{Sr}_x\text{CuO}_4$  (LSCO), showed that in the normal state above the superconducting transition the rotational symmetry of the electron fluid is broken; while the average crystal structure is pinned to the substrate (i.e.,  $\text{C}_4$ -symmetric), the electronic resistivity appears orthorhombic ( $\text{C}_2$ -symmetric)<sup>21</sup>. Hence, the high-temperature superconductivity (HTS) in LSCO emerges out of an electronic nematic state. We have elucidated the temperature and doping dependence of both the director and amplitude of the nematic order in LSCO films, and have shown that in the vicinity of optimum doping the nematic director switches its orientation upon entering the temperature range in which superconducting fluctuations become substantial. This peculiar effect is a manifestation of the interplay between nematicity and (unconventional) superconductivity. Indeed, signatures of electronic nematicity have also been detected in several other strongly-correlated materials and by other experimental techniques, including electronic transport measurements<sup>8-14,17,20,21</sup>, optical spectroscopy<sup>19</sup>, spectroscopic scanning tunneling microscopy<sup>15,18</sup>, angle-resolved photoemission spectroscopy<sup>23,26</sup>, etc.

The main experimental challenge stems from the fact that in most materials the amplitude of nematicity is relatively small, typically just a few percent of the physical quantity under study. For example, the in-plane anisotropy<sup>21</sup> in longitudinal resistivity in optimally-doped LSCO films at room temperature is  $\sim 2\%$ . It is experimentally challenging to accurately measure such a small difference signal on top of a relatively large background. More important, the common practice is to judge about the presence or absence of electronic nematicity from the measurement of some physical property — such as the electrical resistivity — along two orthogonal principal crystal directions. However, although

this fact is not universally realized and appreciated, this is in general not sufficient, because the director of the nematicity need not be aligned with the crystal lattice. This will be illustrated in the next section.

## 2. Van der Pauw Method

The standard technique to determine the electrical resistivity in single crystals or thin films is the Van der Pauw method. This method can be generalized to measure the anisotropy in the longitudinal resistivity along two orthogonal directions<sup>28</sup>. However, this method has some disadvantages, limiting its applicability in the measurements of the electronic nematicity. For one, in this method it is a prerequisite that the principal directions of the resistivity tensor are known. However, the director of nematicity need not be aligned with any of the principal crystallographic directions, and it is in general unknown for a new material. Simply assuming that the crystal axes coincide with the principal directions of the resistivity tensor may lead to quantitatively and qualitatively inaccurate conclusions.

To appreciate this, consider a hypothetical material in which the in-plane resistivity has the orthorhombic symmetry, such that the direction of the highest-resistivity  $\rho_{\max}$  is along  $[110]$ , and the lowest-resistivity direction  $\rho_{\min}$  is along  $[-110]$ . However, no matter how big the actual difference really is between  $\rho_{\max}$  and  $\rho_{\min}$ , if one only measures the resistivities  $\rho_a$  along  $[100]$  and  $\rho_b$  along  $[010]$ , indeed one will find that  $\rho_a = \rho_b$ , and (erroneously) conclude that the material has tetragonal symmetry and is therefore not nematic. This situation is not merely hypothetical; in fact, this is exactly what happens in optimally doped LSCO at room temperature. The point here is that to properly characterize the nematic order it is in general necessary to perform measurements at varied in-plane angles, and accurately determine the nematic director orientation.

The second disadvantage of the Van der Pauw method is that the physical quantity it provides is the longitudinal resistivity, which is a much less sensitive indicator of the electronic nematicity than the transverse resistivity, as we show next.

### 3. Angle-Resolved Transverse Resistivity Method

To meet these challenges, we have developed the Angle-Resolved Transverse Resistivity (ARTR) method<sup>21,24</sup>. The technique is conceptually quite simple, and it is based on the fact that transverse voltage may arise solely due to an anisotropic resistivity.

In general,  $\mathbf{E} = \rho \mathbf{J}$ , where  $\mathbf{E}$  is the electric field,  $\rho$  the resistivity tensor, and  $\mathbf{J}$  the electric current density. In what follows, we consider only the in-plane properties. If the material is tetragonal, i.e., it has  $\mathbf{C}_4$  rotational symmetry, the resistivity tensor is diagonal:

$$\rho = \begin{pmatrix} \rho & 0 \\ 0 & \rho \end{pmatrix},$$

in every system of orthogonal coordinates, because the eigenvalue  $\rho$  is twofold degenerate, and every in-plane vector is an eigenvector. For an orthorhombic material, the resistivity tensor can also be diagonalized as:

$$\rho = \begin{pmatrix} \rho_a & 0 \\ 0 & \rho_b \end{pmatrix},$$

but only in the coordinate system  $(\mathbf{e}_a, \mathbf{e}_b)$  defined by the principal axes, which we assume to coincide with the crystallographic  $[1\ 0\ 0]$  and  $[0\ 1\ 0]$  directions, respectively. However, if we rotate the coordinate system away from the principal axes, the off-diagonal matrix elements must be non-zero, as we show next.

To simplify the notation, let us introduce  $\bar{\rho} = (\rho_a + \rho_b)/2$  and  $\Delta\rho = (\rho_a - \rho_b)/2$ . If the coordinate system is rotated by an angle  $\phi$ , so that  $\mathbf{e}_x = \hat{\mathbf{C}}_\phi \mathbf{e}_a$  and  $\mathbf{e}_y = \hat{\mathbf{C}}_\phi \mathbf{e}_b$ , the matrix  $\rho$  in the coordinate system  $(\mathbf{e}_x, \mathbf{e}_y)$  becomes:

$$\hat{\mathbf{C}}_\phi \rho \hat{\mathbf{C}}_\phi^{-1} = \begin{pmatrix} \cos\phi & -\sin\phi \\ \sin\phi & \cos\phi \end{pmatrix} \begin{pmatrix} \rho + \Delta\rho & 0 \\ 0 & \rho - \Delta\rho \end{pmatrix} \begin{pmatrix} \cos\phi & \sin\phi \\ -\sin\phi & \cos\phi \end{pmatrix} = \begin{pmatrix} \rho + \Delta\rho \cos(2\phi) & \Delta\rho \sin(2\phi) \\ \Delta\rho \sin(2\phi) & \rho - \Delta\rho \cos(2\phi) \end{pmatrix}$$

while  $\mathbf{E} = \begin{pmatrix} E_x \\ E_y \end{pmatrix}$  and  $\mathbf{J} = \begin{pmatrix} J_x \\ J_y \end{pmatrix}$ .

If the film is patterned into a Hall bar oriented in such a way that the current is constrained to flow along  $\mathbf{e}_x$ , we get  $\mathbf{J} = \begin{pmatrix} J \\ 0 \end{pmatrix}$  and consequently

$$E_x / J = \rho_{xx} = \bar{\rho} + \Delta\rho \cos(2\phi) \quad (1)$$

$$E_y / J = \rho_{xy} = \Delta\rho \sin(2\phi) \quad (2)$$

Therefore, a spontaneous transverse voltage must occur in every orthorhombic material, as long as the current is not aligned with one of the principal axes. Moreover, this spontaneous transverse voltage must show the  $\sin(2\phi)$  angular dependence. Since this occurs without any applied magnetic field, this transverse voltage is unrelated to normal or anomalous Hall effect, ferromagnetism, orbital antiferromagnetism, Rashba spin-orbit coupling, Berry phase, etc. Here, the sole origin of the transverse voltage is the anisotropy of the resistivity. Simply speaking, the current will flow along the highest-conductivity direction rather than along the applied external field, unless it is constrained otherwise by the device geometry and orientation.

Note also, from equation (1), that the longitudinal resistivity  $\rho$  must also show oscillations, of the same amplitude and period, just phase-shifted by  $45^\circ$ .

Indeed, our transport measurements in LSCO films fully confirmed these expectations. The films were grown by atomic-layer-by-layer molecular beam epitaxy method (ALL-MBE) that has been amply demonstrated to produce the highest-quality, single-crystal thin films of LSCO<sup>21,29-40</sup>. These MBE-grown films are very uniform in thickness and composition, which is important to eliminate or at least minimize possible extrinsic symmetry-breaking factors. All LSCO films were verified by high-resolution x-ray diffraction to be essentially tetragonal in their average structure, which is indeed expected since the films are very thin and epitaxially constrained to the strictly tetragonal LaSrAlO<sub>4</sub> substrates.

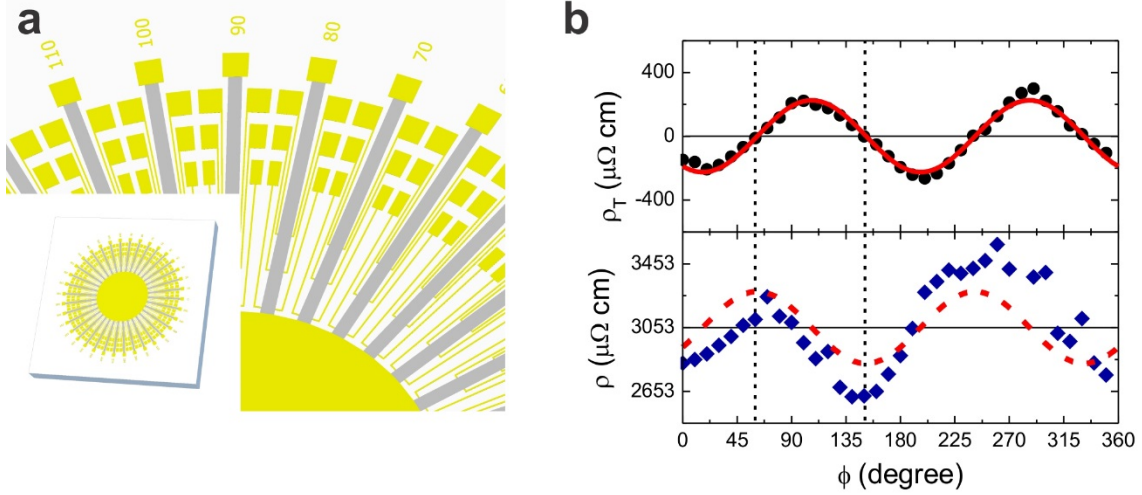


**Figure 1** | **a**, The lithography pattern used for the ‘sun-beam’ ARTR method. The current runs along one of the Hall bars (grey); the voltages are recorded along and transverse to the bar. The inset shows the complete sunbeam containing 36 Hall bars. **b**, The measured angular dependence of  $\rho_T$  and  $\rho$  on the angle  $\phi$  for a  $\text{La}_{1.96}\text{Sr}_{0.04}\text{CuO}_4$  thin film at  $T = 295$  K. The black dots and the blue diamonds indicate the experimental data. The solid red line is the best fit to the expression  $\rho_T^0 \sin[2(\phi - \alpha)]$ , where  $\rho_T^0$  and  $\alpha$  are the fitting parameters. The dotted line was obtained by shifting the solid red line by  $45^\circ$  to the left and up by  $\bar{\rho}$ , the angular average of  $\rho(\phi)$ . The dotted red line agrees with the measured  $\rho(\phi)$  values reasonably well, without any adjustments.

In Fig. 1a, we show the ‘sun-beam’ lithography pattern used in these experiments. It consists of 36 Hall bars (colored in grey), arranged in  $10^\circ$  steps. The current is passed through one Hall bar at a time, and the longitudinal and transverse voltages are measured between the respective contacts. The experimental data, mapping out  $\rho_T(\phi)$  and  $\rho(\phi)$  for  $\phi$  from  $0^\circ$  to  $350^\circ$ , are shown in Fig. 1b. Also shown are the fits to the equations (1) and (2). To make the case most strongly, we have fitted just  $\rho_T(\phi)$  to the expression  $\rho_T^0 \sin[2(\phi - \alpha)]$ , in which  $\rho_T^0$  and  $\alpha$ , the amplitude and the phase offset of oscillations, respectively, are the free fitting parameters. The solid red curve in the upper panel of Fig. 1b shows this fit. In the lower panel of Fig. 1b, the dashed red line is *not* an independent fit of  $\rho(\phi)$  to the expression  $\bar{\rho} + \Delta\rho \cos[2(\phi - \alpha)]$ . Rather, it is the same curve as the one in the upper panel, just offset up by  $\bar{\rho}$  and left by  $45^\circ$ . Apparently, it agrees reasonably well with the measured  $\rho(\phi)$  data.

Thus, the ARTR method outlined above allows for precise measurement of the amplitude and the director of the nematic order. Note that the ARTR method is much more sensitive — typically by an order of magnitude or more — than just measuring  $\rho(\phi)$ . The reason for this can be seen in the equations (1) and (2). If the orthorhombicity  $\Delta\rho$  is relatively small, the oscillations in  $\rho(\phi)$  may be buried within the noise, i.e., within the device-to-device variations in the ‘background’  $\bar{\rho}$  due to lithography, nonuniformity in the film composition or thickness, etc. However,  $\rho_T(\phi)$  is background-free; if the material is tetragonal  $\rho_T(\phi)$  must be identically zero at every angle  $\phi$ . If the material is orthorhombic,  $\rho_T(\phi)$  is in general non-zero and must change sign four times, so one just needs to count the nodes.

#### 4. ARTR without lithography

Indeed, the ARTR method as described in the previous section brings in its own technical challenges. It works the best if the film is of uniform thickness and composition, and if the lithography is perfect enough not to introduce any artifacts.

To address these potential issues, we have explored an alternative, lithography-free variant of the ARTR method. As shown in Fig. 2a, we deposit Au contact pads through a micromachined shadow mask. The transverse resistance  $R_T$  is measured in a ‘cross’ geometry, e.g. by running the current from the contact 1 to the contact 2 and measuring the voltage between the contacts 3 and 4. Subsequently,  $R_T(\phi)$  is measured at other angles by rotating the ‘cross’ in  $10^\circ$  steps and repeating the measurements. To verify the effectiveness of this method, we studied a  $\text{La}_{1.96}\text{Sr}_{0.04}\text{CuO}_4$  thin film as an example. The measured  $R_T(\phi)$  is shown in Fig. 2b. This film has exactly the same doping as the one studied by the ARTR method in Fig. 1, so we can directly compare the results of the two techniques. The clear angular oscillation in  $R_T(\phi)$  seen in Fig. 2b are similar to the oscillation in  $\rho_T(\phi)$  in Fig. 1.

On the other side, note that in the present case of the film that is not patterned, the current distribution between contacts (e.g. the contacts 1 and 2), is not spatially uniform. For this reason, to interpret the  $R_T(\phi)$  data correctly — i.e., to extract the corresponding  $\rho_T(\phi)$  —

it is necessary to self-consistently model the current distribution in the presence of the electronic anisotropy.

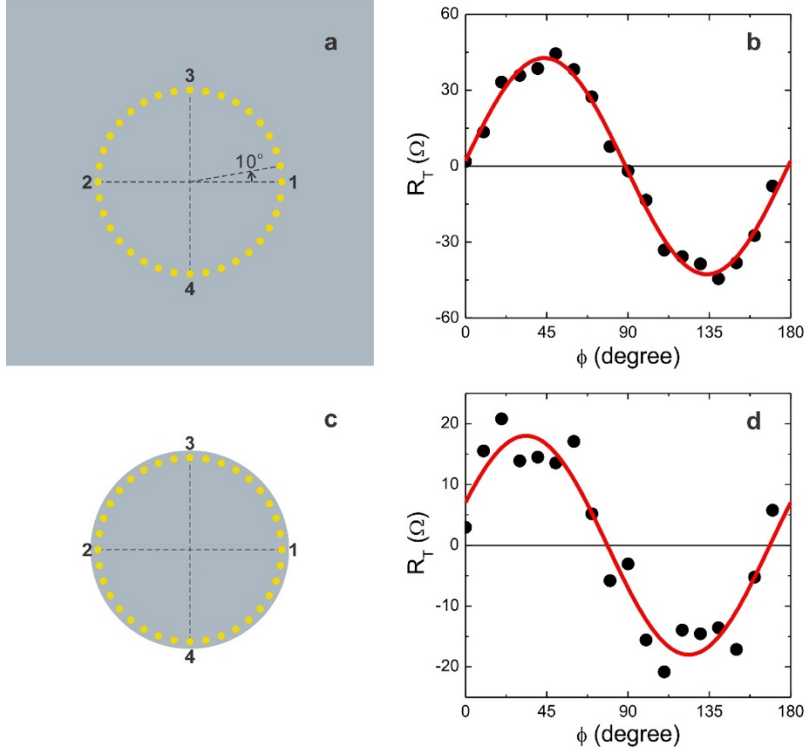


**Figure 2** | Lithography-free ARTR measurements of the electronic nematicity in  $\text{La}_{1.96}\text{Sr}_{0.04}\text{CuO}_4$  thin film at  $T = 295$  K. **a**, The yellow circles are Au contact pads deposited through a micromachined shadow mask. Every Au contact is a circle with a diameter of 0.2 mm. A total of 36 Au contacts are arranged in a circle of diameter 5 mm. The grey square is the LSCO film,  $10 \times 10 \text{ mm}^2$ . The transverse resistance  $R_T$  was measured by recording the voltage difference transverse to the current direction, e.g. the current runs from the contact 1 to 2 and the voltage is measured between the contacts 3 and 4. **b**, The measured  $R_T(\phi)$  shows a clear angular oscillation, consistent with the results in Fig. 1. The black dots are the experimental data and the red curve is the best fit to the function  $R_T = R_T^0 \sin [2(\phi - \alpha)]$ , where  $R_T^0$  and  $\alpha$  are free parameters. **c**, The same as in the panel **a** except that the film outside of the grey circle was etched away. The diameter of the grey circle is 5.5 mm. **d**,  $R_T(\phi)$  measured in the circular sample shown in panel **c**. The difference between the amplitudes and the phase offsets of the oscillations in  $R_T(\phi)$  shown in the panels **b** and **d**, respectively, illustrate how removing the film area outside of the grey circle affected the result significantly.

To underscore this, we etched away a portion of this LSCO film, the area surrounding the grey circle in Fig. 2c. While the sample geometry has been modified, from a square to a

circle,  $R_T(\phi)$  still showed clear angular oscillations, see Fig. 2d, indicating that the electronic nematicity is intrinsic to LSCO. However, the amplitude and the phase offset of the oscillation changed significantly from that in Fig. 2b. This is due to the fact that by removing some of the LSCO film, the surrounding area outside the grey circle, we have restricted the current to run only inside the circle, and thus altered the current flow pattern. The change in the phase of oscillations originates from this change in the film geometry. In Fig. 2a, the film is square-shaped, which would make  $R_T(\phi)$  to oscillate even if  $\rho_T(\phi)$  were isotropic. If the current runs between the contacts 1 and 2 at  $\phi = 0^\circ$ , the geometry of the experiment has a reflection-plane symmetry, while this is not true for  $\phi = 10^\circ, 20^\circ$ , etc. In contrast, the circle-shaped geometry of film in Fig. 2c does not favor a specific direction. For this reason, circle-shaped samples are preferable, as they do not introduce external asymmetry to the experimental arrangement.

To extract the amplitude and the director orientation from the measured  $R_T(\phi)$  data, one needs some numerical modeling. Apart from taking into account the geometry of the sample, the model also needs to include the effect of the nematicity self-consistently. For example, one can start by first assuming a trial nematic order, i.e., some function  $\rho(\phi)$ , calculate the current distribution based on this assumption as the input, and calculate  $R_T(\phi)$  based on this model. Then one can systematically iterate the amplitude and the phase of nematicity until the best fit to the experimental  $R_T(\phi)$  data is achieved. The whole process is somewhat sophisticated and in general requires extensive numerical simulations. Our first ARTR method, based on the sun-beam pattern, is much simpler and more direct, as long as thin film samples are concerned.

However, for bulk single crystals, lithographic patterning is in general not feasible, and then this lithography-free ARTR technique may be the method of choice. We illustrate this using a  $\text{La}_{1.93}\text{Sr}_{0.07}\text{CuO}_4$  bulk crystal as an example. The single crystal was cut into thin disks 6 mm in diameter and 2 mm in thickness. For this experiment, the polished surface of the crystal was deliberately tilted by  $14^\circ$  away from the  $a$ - $c$  plane, as confirmed by the Laue X-ray diffraction. Since in LSCO the longitudinal resistivity is approximately two orders of magnitude higher along the  $c$ -axis than within the  $a$ - $b$  plane, in this sample

the dominant factor is the large out-of-plane anisotropy. The effect is large and thus convenient for a proof-of-principle illustration of the method.

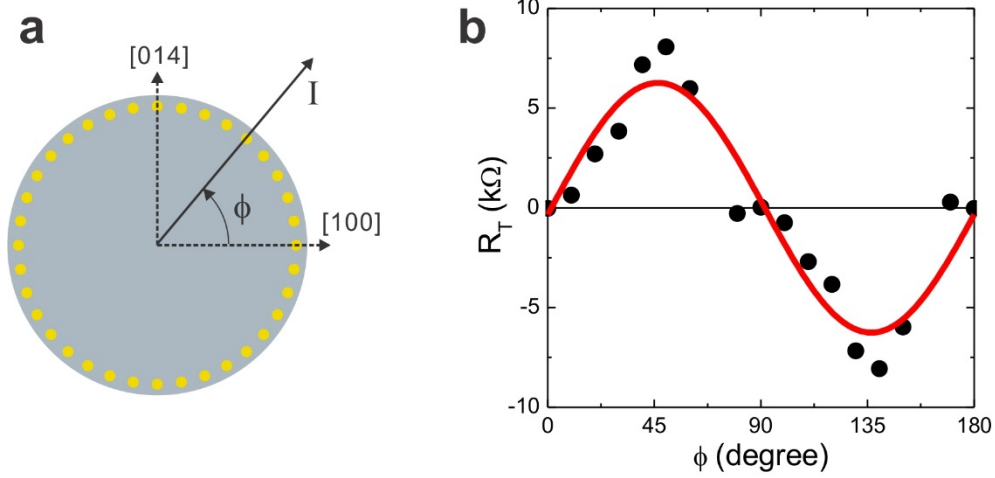


**Figure 3** | Measurements of transport anisotropy in a bulk LSCO single crystal. **a**, The surface of the polished LSCO crystal is tilted by  $14^\circ$  away from the  $a$ - $c$  plane. The crystal  $[1\ 0\ 0]$  direction, i.e., the  $a$ -axis, corresponds to  $\phi = 0^\circ$ . The  $[0\ 1\ 4]$  direction,  $14^\circ$  away from the  $c$ -axis, corresponds to  $\phi = 90^\circ$ . The orientation between the two current contacts is denoted by  $I$ . **b**,  $R_T(\phi)$  shows a strong angular oscillation that originates from the uniaxial anisotropy in transport. The black dots are the experimental data, and the red curve is the fit to the function  $R_T = R_T^0 \sin [2(\phi - \alpha)]$ .

The measured transverse resistance data, Fig. 3, are well fitted by  $R_T = R_T^0 \sin [2(\phi - \alpha)]$ , where  $R_T^0$  and  $\alpha$  are free parameters. From the fit, we get  $\alpha = 0^\circ$ . According to our equations (1) and (2), the angle at which the transverse resistivity is zero must coincide with the angle at which the longitudinal resistivity is at the maximum or the minimum, given the  $45^\circ$  phase shift between the oscillations in these two quantities. In this single crystal, the minimum longitudinal resistivity is along the  $a$ -axis of the crystal, i.e., at  $\phi = 0^\circ$ . This means that the node in the angular oscillations of  $R_T$  should be at  $\phi = 0^\circ$ , consistent with our measured phase offset  $\alpha = 0^\circ$ . This is another piece of evidence confirming that this method is applicable to bulk-crystal samples. The remaining challenge, however, is to determine the current distribution between each pair of current contacts and retrieve the exact magnitude of anisotropy. As discussed above, this demands substantial modeling and calculations, so it is not our favored option.

Another technique applicable to bulk crystals is to use focused ion beam (FIB) and pattern the crystal into a Hall-bar geometry. In this way, the current flow is restricted by the geometry of the device, and is distributed uniformly across the device. However, the throughput and the efficiency of this method are fairly low. For every in-plane angle, a different device needs to be fabricated, sequentially, thus consuming significant amounts of FIB time. Thus, in practice the FIB method is only used to measure  $R(\phi)$  and  $R_T(\phi)$  at several chosen angles  $\phi$ , and it should preferably be complemented by other techniques and measurements.

## **Summary**

We have described several transport methods to probe the anisotropy and nematicity in thin films and bulk single crystals. We discussed in detail the advantages and disadvantages of each technique. We used LSCO as the example material, but we emphasize that the same methods are easily applicable to other classes of materials. Further investigations of nematicity in strongly correlated materials should advance our understandings of this interesting novel phenomenon. It may not be a mere coincidence that every unconventional superconductor studied so far was also found to host electronic nematicity in the normal state; we speculate that the breaking of rotational symmetry disfavors s-wave pairing and promotes unconventional superconductivity. To (dis)prove this conjecture is now one of the grand challenges to the Condensed Matter Physics community.

## **Acknowledgements**

The research at Brookhaven National Laboratory was supported by the U.S. Department of Energy, Basic Energy Sciences, Materials Sciences and Engineering Division. X.H. was supported by the Gordon and Betty Moore Foundation's EPiQS Initiative through Grant GBMF4410.

## References

1. Kivelson, S.A., Fradkin, E., Emery, V.J.: Electronic liquid-crystal phases of a doped Mott insulator. *Nature* **393**, 550–553 (1998)
2. Oganesyan, V., Kivelson S.A., Fradkin, E.: Quantum theory of a nematic Fermi fluid. *Phys. Rev. B* **64**, 195109 (2001)
3. Zaanen, J., Nussinov, Z., Mukhin, S.I.: Duality in 2+1D quantum elasticity: Superconductivity and quantum nematic order. *Annals of Physics* **310**, 181–260 (2004)
4. Fradkin, E., Kivelson, S.A., Lawler, M.J., Eisenstein, J.P., Mackenzie, A.P.: Nematic Fermi fluids in condensed matter physics. *Annu. Rev. Condens. Matter Phys.* **1**, 153–78 (2010)
5. Carlson, E.W., Dahmen, K.A.: Using disorder to detect locally ordered electron nematics via hysteresis. *Nature Commun.* **2**, 379 (2011).
6. Phillabaum, B.V., Carlson, E.W., Dahmen, K.A.: Spatial complexity due to bulk electronic nematicity in a superconducting underdoped cuprate. *Nature Commun.* **3**, 915 (2011)
7. Beekman, A.J., et al.: Dual gauge field theory of quantum liquid crystals in two dimensions. *Physics Reports* **683**, 1-110 (2017)
8. Lilly, M.P., Cooper, K.B., Eisenstein, J.P., Pfeiffer, L.N., West, K.W.: Evidence for an anisotropic state of two-dimensional electrons in high Landau levels. *Physical Review Letters* **82**, 394–97 (1999)
9. Du, R.R., et al.: Strongly anisotropic transport in higher two-dimensional Landau levels. *Solid State Communications* **109**, 389 (1999)
10. Borzi R.A., et al.: Formation of a nematic fluid at high fields in  $\text{Sr}_3\text{Ru}_2\text{O}_7$ . *Science* **315**, 214–17 (2007)
11. Ando, Y., Segawa, K., Komiya, S., Lavrov, A.N.: Electrical resistivity anisotropy from self-organized one dimensionality in high-temperature superconductors. *Physical Review Letters* **88**, 137005 (2002)
12. Abdel-Jawad, M., et al.: Anisotropic scattering and anomalous normal-state transport in a high-temperature superconductor. *Nature Physics* **2**, 821–825 (2006)
13. Hinkov, V., et al.: Electronic liquid crystal state in the high-temperature superconductor  $\text{YBaCuO}$ . *Science* **319**, 597-600 (2008)
14. Daou, R., et al.: Broken rotational symmetry in the pseudogap phase of a high- $T_c$  superconductor. *Nature* **463**, 519-522 (2010)
15. Lawler, M.J., et al.: Intra-unit-cell electronic nematicity of the high- $T_c$  copper-oxide pseudogap states. *Nature* **466**, 347–351 (2010)
16. Li, L., Alidoust, N., Tranquada, J.M., Gu, G.D., Ong, N.P.: Unusual Nernst effect suggesting time-reversal violation in the striped cuprate superconductor LBCO. *Physical Review Letters* **107**, 277001 (2011)

17. Mesaros, A., et al.: Topological defects coupling smectic modulations to intra-unit-cell nematicity in cuprates. *Science* **333**, 426-430 (2011)
18. Fujita, K., et al.: Simultaneous transitions in cuprate momentum-space topology and electronic symmetry breaking. *Science* **344**, 612-616 (2014)
19. Lubashevsky, Y., Pan, L.D., Kirzhner, T., Koren, G., Armitage, N.P.: Optical birefringence and dichroism of cuprate superconductors in the THz regime. *Phys. Rev. Lett.* **112**, 147001 (2014)
20. Cyr-Choinière, O., et al. : Two types of nematicity in the phase diagram of the cuprate superconductor  $\text{YBa}_2\text{Cu}_3\text{O}_y$ . *Phys. Rev. B* **92**, 224502 (2015)
21. Wu, J., Bollinger, A.T., He, X., Božović, I.: Spontaneous breaking of rotational symmetry in copper oxide superconductors. *Nature* **547**, 432–435 (2017)
22. Zhang, J.-C., et al.: Anomalous thermal diffusivity in underdoped  $\text{YBa}_2\text{Cu}_3\text{O}_{6+x}$ . *PNAS USA* **114**, 5378-5383 (2017)
23. Zhao, L., et al.: Global inversion-symmetry-broken phase inside the pseudogap region of  $\text{YBa}_2\text{Cu}_3\text{O}_y$ . *Nature Physics* **13**, 250–254 (2017)
24. Wu, J., Bollinger, A.T., He, X., Božović, I.: Detecting electronic nematicity by the angle-resolved transverse resistivity measurements. *J. Supercond. Nov. Magn.* <https://doi.org/10.1007/s10948-018-4885-3> (2018)
25. Fernandes, R.M., Chubukov, A.V., Schmalian, J.: What drives nematic order in iron-based superconductors? *Nature Physics* **10**, 97–104 (2014)
26. Johnson, P.D., et al.: Spin-orbit interactions and the nematicity observed in the Fe-based superconductors. *Physical Review Letters* **114**, 167001 (2015)
27. Avci, S., et al.: Magnetically driven suppression of nematic order in an iron-based superconductor. *Nature Communications* **5**, 3845 (2014)
28. Montgomery, H.C.: Method for measuring electrical resistivity of anisotropic materials. *J. App. Phys.* **42**, 2971-2975 (1971)
29. Bozovic, I., et al.: Epitaxial strain and superconductivity in  $\text{La}_{2-x}\text{Sr}_x\text{CuO}_4$  thin films. *Phys. Rev. Lett.* **89**, 107001-4 (2002)
30. Bozovic, I., et al.: No mixing of superconductivity and anti-ferromagnetism in a high-critical-temperature superconductor. *Nature* **422**, 873-5 (2003)
31. Gozar, A., et al.: Interface superconductivity between a metal and a Mott insulator. *Nature* **455**, 782-5 (2008)
32. Logvenov, G., Gozar, A., Bozovic, I.: High-temperature superconductivity in a single copper-oxygen plane. *Science* **326**, 699–702 (2009).
33. Smadici, S., et al.: Superconducting transition at 38 K in insulating-overdoped  $\text{La}_2\text{CuO}_4$ - $\text{La}_{1.64}\text{Sr}_{0.36}\text{CuO}_4$  superlattices: evidence for interface electronic redistribution from resonant soft X-Ray scattering. *Phys. Rev. Lett.* **102**, 107004 (2009)
34. Bollinger, A.T., et al.: Superconductor–insulator transition in  $\text{La}_{2-x}\text{Sr}_x\text{CuO}_4$  at the pair quantum resistance. *Nature* **472**, 458-460 (2011)

35. Dean, M. P. M., et al.: Spin excitations in a single  $\text{La}_2\text{CuO}_4$  layer. *Nature Materials* **11**, 850-4 (2012)
36. Dean, M. P. M., et al.: Persistence of magnetic excitations in  $\text{La}_{2-x}\text{Sr}_x\text{CuO}_4$  from the undoped insulator to the heavily overdoped non-superconducting metal. *Nature Materials* **12**, 1019-23 (2013)
37. Wu, J., et al.: Anomalous independence of interface superconductivity on carrier density. *Nature Materials* **12**, 877-881 (2013)
38. Božović, I., He, X., Wu, J., Bollinger, A.T.: Dependence of critical temperature in overdoped copper oxides on superfluid density. *Nature* **536**, 309-311 (2016)
39. Giraldo-Gallo, P., et al.: Scale invariant magnetoresistance in the strange metal phase of a cuprate superconductor. *Science* **361**, 479-481 (2018)
40. Mahmood, F., He, X., Božović, I., Armitage, N.P.: Locating the missing superconducting electrons in overdoped cuprates. *Phys. Rev. Lett.* **122**, 027003 (2019).